

## Testing Graizer-Kalkan Ground Motion Prediction Model on USGS - Global Atlas Database

Vladimir Graizer, Erol Kalkan, and Kuo-Wan Lin

Corresponding author: Erol Kalkan

Mailing address: Dr. Erol Kalkan, P.E.  
United States Geological Survey  
Western Region Earthquake Hazards Team  
MS977, 345 Middlefield Rd.  
Menlo Park, CA 94025

Phone: (650) 329-5146

Fax: (650) 329-5163

E-mail: [ekalkan@usgs.gov](mailto:ekalkan@usgs.gov)

**Keywords:** Attenuation relationship; Tectonic region; Standard error; Ground motion prediction;  
Seismic hazard

# Testing Graizer-Kalkan Ground Motion Prediction Model on USGS - Global Atlas Database

Vladimir Graizer,<sup>a)</sup> M.EERI, Erol Kalkan,<sup>b)</sup> M.EERI, and Kuo-Wan Lin,<sup>c)</sup>

An alternative approach to ground motion prediction modeling based on representation of attenuation function as a combination of filters was introduced by Graizer & Kalkan (2007). In this model, each filter is a module calibrated separately to represent a certain physical phenomenon on seismic radiation (e.g., magnitude scaling, site-correction, basin effect, directivity, Moho reflection etc.). This modular approach allows to isolate the influence of each phenomenon on prediction of ground motion intensity thus provides an enhanced robustness and stability to ground motion prediction equation (GMPE). In this paper, our GMPE and its modules are tested on USGS – Global Atlas database which has about 14,000 data points from 244 worldwide shallow crustal events including the 2008  $M7.9$  Wenchuan (China) and 2009  $M6.3$  L'Aquila earthquakes (Italy). Comparison of actual data with predictions demonstrates a very good match up to about 100 km for a range of magnitudes ( $M4.2$  -  $7.9$ ). In order to achieve a better fit at far distances ( $>100$  km), where generally a fast attenuation is observed, two coefficients in our original GMPE are modified and a new module is implemented. The resultant GMPE is tested to be used for reliable ground motion predictions from shallow crustal tectonic regions.

## INTRODUCTION

Current GMPEs has inherent regional dependence due to differences in geologic environments and localized ground motion data utilized in their development. This leads to uncertainties in selection of appropriate GMPEs which are the largest contributions to the overall uncertainties of seismic hazard estimates for a region. Thus, there is a need for an efficient and robust GMPE which can be globally applicable to or easily calibrated for shallow crustal tectonic environments. The NGA database was the most complete source of ground motion data compiled

---

<sup>a)</sup> U.S. Nuclear Regulatory Commission, Washington, DC, [vxgl@nrc.gov](mailto:vxgl@nrc.gov)

<sup>b)</sup> U.S. Geological Survey, Menlo Park, CA, [ekalkan@usgs.gov](mailto:ekalkan@usgs.gov) (*corresponding author*)

<sup>c)</sup> U.S. Geological Survey, Golden, CO, [klin@usgs.gov](mailto:klin@usgs.gov)

from tectonic regions similar to the Western U.S. to generate GMPEs. This database has over 3000 data points; more than 500 of which are from the 1999 Chi-Chi (Taiwan) earthquake and the majority of the rest are from the Californian events. The NGA database with a number of additions (e.g., 2003 San Simeon and 2004 Parkfield earthquakes in California) was used to develop the GK-07 GMPE (Graizer and Kalkan, 2007). The GK-07 well predicts the ground motions recorded not only from the Californian events, but also Denali (Alaska), Chi-Chi, Kocaeli and Düzce (Turkey) earthquakes. The GK-07 is originally designed to represent attenuation function as a combination of filters where each filter is a module calibrated separately to represent a certain physical phenomenon on seismic radiation (e.g., magnitude scaling, site-correction, basin effect, directivity, Moho reflection etc.). This approach isolates the influence of each phenomenon on prediction of ground motion intensity, thus provides an enhanced robustness and stability to GMPE. In this paper, the GK-07 and its modules are comprehensively tested using the USGS – Global Atlas database. Also examined here is its applicability to far distances ( $R_{cl} > 200$  km, where  $R_{cl}$  is closest fault distance – perpendicular distance between site and fault's surface projection) up to about 500 km. Ground motion prediction at distances more than 200 km has a particular interest for nuclear industry.

### USGS - ATLAS GLOBAL GROUND MOTION DATABASE

The USGS – Atlas global database (<http://earthquake.usgs.gov/eqcenter/shakemap/atlas.php>) contains mixture of data from different tectonic environments. The primary sources for strong-motion data are from: (1) Pacific Earthquake Engineering Research Center's NGA database ([http://peer.berkeley.edu/products/nga\\_project.html](http://peer.berkeley.edu/products/nga_project.html)), (2) Consortium of Organizations for Strong-Motion Observation Systems (<http://db.cosmos-eq.org/scripts/default.plx>), (3) European Strong-Motion database (<http://www.isesd.hi.is/>), and (4) Kyoshin Network (K-NET) (<http://www.k-net.bosai.go.jp/>). Table 1 presents all crustal events in our database with their relevant information on magnitude and style of faulting; also listed are the breakdowns of record numbers from each event. Among the totaling 13,992 records used in this study, 7909 records are from reverse faults, 2944 from strike-slip faults, 1285 are from normal faults, and 1854 have undefined faulting mechanism. The distributions of peak ground acceleration (PGA) data against moment magnitude (denoted as  $M$  or  $M_w$ ),  $R_{cl}$ , average shear-wave velocity in the upper 30 m ( $V_{S30}$ ), and style of faulting are shown in Figure 1. As compared to the NGA database, the compiled dataset is more complete not only at far-field but also at near-field; it is also more

inclusive in terms of geologic environment and magnitude range covered. The latest entities are the *M*7.9 Wenchuan (China) earthquake of May 12, 2008 and the *M*6.3 L’Aquila (Italy) earthquake of April 9, 2009. The current set includes PGA (>0.001g) data recorded within 500 km of earthquakes with a magnitude between 4.2 and 7.9.

### GRAIZER-KALKAN GROUND MOTION PREDICTION MODEL

In general, ground motion (*GM*) prediction can be approximated as:

$$GM = f(M, R, C) \quad (1)$$

where *M* is a magnitude *R* is a distance, and *C* is a set of other independent parameters representing for instance style of faulting, shallow site, basin, directivity, and other physical effects. According to Campbell (2003) an attenuation relation in its most fundamental form can be described by the following expression:

$$\ln(GM) = c_1 + c_2 M - c_3 \ln R + c_4 R + c_5 F + c_6 S + \sigma \quad (2)$$

where *F* is a parameter characterizing style of faulting, *S* is a parameter characterizing the local site condition,  $\sigma$  is a random error term with zero mean (i.e., normally distributed). Most GMPE developers are using an approach based on Eq. (2), e.g., Abrahamson and Silva, Boore and Atkinson, Campbell and Bozorgnia, Chiou and Youngs, Idriss; 2008. The shift from Eq. (1) to Eq. (2) represents a shift from linear to logarithmic domain. Since ground motion data is lognormally-distributed, an advantage of this shift to simplify data-fitting through regression by linearization. On the other hand, it pushes researchers to search for a fixed functional form between logarithm of ground motion parameter (e.g., PGA) and magnitude, distance and other independent parameters suitable for both near- and far-field. Let’s look at the consequences of this approach and consider this type of representation from both theoretical and empirical data fitting point of view. This type of representation assumes an exponential approximation of ground motion attenuation, actually a restricted type of representation. The following question can be asked: Is ground motion attenuation exponential? From the wave propagation theory we know that residual displacements attenuate as  $R^{-2}$ , *P*- and *S*-waves attenuate as  $R^{-1}$  and surface waves attenuate as  $R^{-0.5}$  (e.g., Chinnery, 1961; Haskell, 1969), it means that theoretically ground motion attenuation follows a power law.

Now let’s look at how ground motion attenuates at near-field of an earthquake. Spatial distribution of ground motion data recorded in the proximity of earthquake fault zones (e.g.,

Mogul 2008, Parkfield 2004, Chi-Chi 1999, Northridge 1994, Loma Prieta 1989 and Imperial Valley 1979) revealed important attenuation characteristics of PGA as:

- (1) PGA remains constant in the near-field (flat region),
- (2) it exhibits an increase in amplitude (bump on attenuation curve) or a turning point (sharp decay) at certain distances (about 3-10 km from the fault rupture),
- (3) it attenuates with a slope of  $R^{-1}$  and faster at far distances ( $R_{cl} > 100$  km),
- (4) its amplitude amplifies at certain distances due to basin effect or reflection from the Moho surface,
- (5) depending upon characteristic of the crust, it can attenuate much faster at large distances due to regional low Q-values as in the Western U.S.

As shown in Figure 2a, the 2004  $M6.0$  Parkfield earthquake presents an excellent example of a well recorded event at both near- and far-field. It is evident that an exponential attenuation curve with a constant attenuation rate can not be a best fit – not satisfying our observations from near- and far-field ground motion attenuation characteristics (as discussed above).

We are interested in understanding how elasticity and anelasticity in the earth cause the attenuation of propagating waves. This behavior is an example of the general case of how a damped harmonic single-degree-of-freedom (SDF) oscillator responds to a driving force that depends on frequency. Indeed, attenuation characteristic of the Parkfield data is similar to the frequency response function of a SDF oscillator: flat response at the beginning, possible bump and a turning point, and sharp decay. The frequency response function of a SDF oscillator can be expressed as:

$$G(\lambda) = A \left[ (1 - \lambda^2)^2 + 4D_0^2 \lambda^2 \right]^{-0.5} \quad (3)$$

where  $\lambda = \omega/\omega_0$ , and  $A$  is amplification coefficient (i.e., scaling parameter),  $\omega$  is cyclic frequency and  $\omega_0$  is natural cyclic frequency.  $D_0$  is a damping term. Substituting square of frequency ( $\omega^2$ ) term with distance ( $R_{cl}$ ) term, we obtain the “core attenuation equation” of Graizer-Kalkan GMPE as:

$$G(M, R_{cl}, C_0) = \left[ \left[ 1 - (R_{cl}/R_0) \right]^2 + 4D_0^2 (R_{cl}/R_0) \right]^{-0.5} \quad (4)$$

We also suggest using the following mathematical formulation instead of Eq. (2) to represent a GMPE since in this representation each function ( $G_n$ ) is in multiplication form (cascade of filters) helping to better understand their influence on resultant *GM* intensity.

$$PGA = G_1(M, F) \cdot G_2(M, R_{cl}, C_2) \cdot G_3(M, R_{cl}, C_3) \cdot G_4(M, C_4) \cdot G_5(M, R_{cl}, C_5) \cdot G_6(M, R_{cl}, C_6) \cdot \sigma_{PGA} \quad (5)$$

Eq. (5) can be expressed in logarithmic space as:

$$\begin{aligned} \ln(PGA) = & \ln[G_1(M, F)] + \ln[G_2(M, R_{cl}, C_2)] + \ln[G_3(M, R_{cl}, C_3)] + \ln[G_4(M, C_4)] \\ & + \ln[G_5(M, R_{cl}, C_5)] + \ln[G_6(M, R_{cl}, C_6)] + \sigma_{\ln PGA} \end{aligned} \quad (6)$$

What are the advantages of using separate functions ( $G_n$ ) in GMPE and modeling ground motion attenuation by means of a SDF response function?

- It utilizes the idea of modular/filter design, where frequency is simply substituted with distance term.
- It allows presenting each physical phenomena on seismic radiation by a separate filter as a function of meaningful physical independent parameters e.g.,  $M, R_{cl}$ .
- It eliminates need to search for a complex and purely empirical equation working for different tectonic environments and distance ranges.
- Instead of fitting a pre-defined empirical equation to entire dataset via single or two-stage nonlinear regression, each module individually is optimized based on actual data thus provides more stability and robustness.
- It is easy to calibrate each module separately to adjust the GMPE for different tectonic regions.
- It brings more physical meaning to each module, and consequently more connection to theoretical seismology.

In this modular approach, the first module  $G_1$  is for magnitude and style of faulting scaling,  $G_2$  (also called here “core attenuation equation”) models attenuation of ground motion in the near-field (see Figs. 2 and 3).  $G_3$  represents intermediate distance correction and basin effect (if basin presents).  $G_4$  is for ground motion amplification due to shallow site conditions (described later), and  $G_5$  adjusts the slope of attenuation curve at far distances. Amplification of ground motion at intermediate distances due to reflections from Moho surface, near-field directivity and hanging wall effects can also be represented by separate filters. Note that each filter in the GK-07 (see Fig. 3) is a linear or nonlinear function of at least  $M$  and  $R_{cl}$ . The  $G_2$  and  $G_3$  have a corner distance parameter which either defines the distance after which the filter is effective or at which the maximum amplification (bump) associated with this filter takes place (see Fig. 2b).

### ***Physical Interpretation of $R_0$ and $D_0$***

For SDF oscillator,  $f_0$  refers to natural frequency. In our attenuation formulation, it corresponds to a corner distance ( $R_0$ ) where the highest ground motion (bump) or a turning point (change in attenuation rate) is observed.  $R_0$  is clearly a function of earthquake magnitude. It is found that corner distance exhibits a linear function of magnitude as:

$$R_0 = c_4 M + c_5 \quad (7)$$

where  $c_4$  and  $c_5$  are estimator coefficients (Graizer and Kalkan, 2007). Eq. (7) implies that for larger magnitudes, turning point on attenuation curve occurs at far distances ( $> 100$  km). Certain analogy can also be seen between corner distance and the corner frequency in Brune's model (1970, 1971) where corner frequency depends upon the size of the earthquake.

$D_0$  quantifies the intensity of bump on the attenuation curve. It is a function of magnitude reaching minimum with  $D_0 = 0.4$  (producing a significant bump) for  $M6.0 - 6.5$  and being higher at  $M < 5.0$  and  $M > 7.0$  (much lower or no bump).  $D_0$  is defined as:

$$D_0 = c_6 \cos(c_7 M + c_8) + c_9 \quad (8)$$

where  $c_6$ ,  $c_7$ ,  $c_8$  and  $c_9$  are estimator coefficients. Relative level of bump on attenuation curve decreases for larger and smaller magnitudes. For magnitudes larger than 7.5, bump saturates.

### ***Magnitude and Style of Faulting Scaling***

In the initial stage of data fitting for GK-09, variations in site conditions were not distinguished. This stage is essential to obtain main tendencies in the attenuation of ground motion with respect to magnitude. Based on the findings, the following scaling function is developed:

$$A(M, F) = [c_1 \arctan(M + c_2) + c_3] F \quad (9)$$

where  $c_1$ ,  $c_2$  and  $c_3$  are estimator coefficients, and  $F$  represents scaling due to style of faulting. This scaling function reflects saturation of amplitudes of ground motion with increasing magnitudes.

In this study, similar to our original approach, style of faulting is considered to be a simple linear scale factor. According to the results of Sadigh et al. 1997, Campbell and Bozorgnia (in Stewart et al., 2008), reverse-fault events create ground motions approximately 28% higher than those from crustal strike-slip events. Following that, we implemented  $F = 1.00$  for strike-slip and normal faults, and  $F = 1.28$  for reverse faults.

### ***Effect of Shallow Site Conditions***

Based on available studies (a list of references is given in Graizer and Kalkan, 2007), we adopt linear site amplification that can be formulated in natural logarithmic space as

$$F_{site} = b_v \cdot \ln(V_{S30}/V_A) \quad (10)$$

Eq. (10) is the equivalent form of linear site correction expression provided by Boore et al. (1997). In the linear site amplification formula of Boore et al.  $b_v = -0.371$  whereas our estimates yield  $b_v = -0.24$ . Similar to the results of Field (2000), our attenuation model exhibits less amplification as the  $V_{S30}$  decreases compared to stiff site conditions.

Before adopting the linear site amplification filter, we also considered recently developed nonlinear models (e.g., Choi and Stewart, 2005). Cross-comparison of NGA GMPEs demonstrates significant differences in site amplification for PGA and spectral acceleration ordinates especially for soft-soils ( $V_{S30} < 400$  m/sec) (2009 SSA presentation of I.M. Idriss). These significant differences between existing nonlinear models indicate that they need calibration based on experimental data.

### ***Sediment Depth Basin Effect***

Basin effect significantly impacts wave field at distances 30-50 km and more when deep sedimentary basin is present (e.g., Lee et al., 1995; Campbell, 1997; Frankel et al., 2001). In most cases it is associated with large amplitude surface waves. We model this effect by applying the  $G_3$  filter as shown in Figures 2 and 3. Similar to the  $G_2$  filter, the  $G_3$  filter is determined by two parameters: Distance  $R_I$  and damping  $D_I$ . In this case,  $R_I$  describes the distance for bump (amplification due to basin), and  $D_I$  describes its amplitude (lower value of  $D_I$  produces higher amplitudes of bump) (see Fig. 2b). If sediment thickness is low, basin effect can be neglected;  $D_I$  in this case can be taken as 0.65 - 0.70 (no bump). The  $G_3$  filter with this value of  $D_I$  results in a change of slope at distances larger than  $R_I$  only; it remains ineffective for distances less than  $R_I$  (see Fig. 2b). Resultant attenuation function ( $G_2 \cdot G_3$ ) decays proportionally to  $R^{-1.5}$  unlike  $R^{-1}$  decay produced by the  $G_2$  filter as shown in Fig. 2c.

We envision damping parameter of the third filter ( $D_I$ ) to be a smooth function of basin depth (thickness of sediment layer). But in our first approximation, we simply consider basin effect to be same for all depths of sediments ( $Z$ ) more than 1 km deep.

$$G_3(M, R, C_1) = \left[ \left[ 1 - (R/R_1)^{0.5} \right]^2 + 4D_1^2(R/R_1)^{0.5} \right]^{-0.5}$$
$$D_1 = \begin{cases} 0.65 & \text{for } Z < 1 \text{ km} \\ 0.35 & \text{for } Z \geq 1 \text{ km} \end{cases} \quad (11)$$

In general, we expect  $D_1$  to be decreasing smoothly from 0.7 to 0.3-0.4 and saturating with the increase in sediment thickness (we plan to study this effect later).

### ***Moho Reflection***

The path effects on strong ground motion due to crustal structures have been known for a while. Burger et al. (1987) shows that the observed interval of relatively high amplitudes in the distance range of 60 to 150 km in North America can be attributed to post-critically reflected S-waves from the Moho discontinuity. Somerville et al. (1990) found significant influences of critical reflections from the lower crust on ground motion attenuation from the large set of strong-motion records of the 1988 Saguenay, Quebec earthquake at distances between 50 and 120 km. In central California, Bakun and Joyner (1984) suggested that the large positive residuals in  $M_L$  at distances between 75 and 125 km could be due to Moho reflections. Somerville and Yoshimura (1990) presents evidence of enhanced amplitudes of strong ground motion from the 1989 Loma Prieta earthquake recorded at San Francisco and Oakland. Liu and Tsai (2009) showed significant effect of Moho reflection on peak ground motion in Northwestern Taiwan. With the methodology implemented herein, it is possible to add another filter to represent the Moho reflection as  $G_6(M, R, C_6)$ . This filter's behavior is conceptually demonstrated in Figure 2d. The calibration of this filter based on the recorded data is left for a future study.

### ***Far Distance Attenuation Filter***

For distances more than 100 km from the fault (increasing with the increase of the earthquake magnitude) attenuation of ground motion data demonstrate two main tendencies: faster attenuation in the order of  $R^{-4}$ , and slower attenuation in the order of  $R^{-1.5}$ . Analyses show that increase in the attenuation slope and correspondently faster attenuation is associated with the areas of relatively low Q-values, and slower attenuation is associated with the areas with high Q-factors. For regions similar to the Central and Eastern U.S. with relatively high Q-values (Singh and Herrmann, 1983; Mitchell and Hwang, 1987; Chandler et al., 2006), attenuation at far-field is about the same as for near-field (about  $R^{-1.5}$ ). On the other hand, in the Western U.S. with

relatively low Q-values, attenuation is faster (almost  $R^{-4}$ ) at far distances (e.g., 2004 Parkfield earthquake as shown in Fig. 2a).

To model fast attenuation at far distances, the following filter is utilized.

$$G_5(M, R_{cl}, Q) = \left[ (1 - (R_{cl}/R_3)^d)^2 + 4D_3^2(R_{cl}/R_3)^d \right]^{-0.5} \quad (12)$$

$G_5$  has a flat region at distances  $R_{cl} < R_3$ , a turning point around the corner distance  $R_3$  for damping parameter  $D_3 = 0.6\text{-}0.7$ . The slope of attenuation is determined by an adjustable parameter  $d$ . We expect parameter  $d$  and  $G_5$  to be functions of Q-factor  $d(Q)$ , and  $G_5(M, R_{cl}, Q)$ .  $d$  varies from 0 to 2.5, with 0 meaning that no adjustment to the attenuation slope is needed.

For the Atlas dataset which constitutes a mixture of data from different tectonic regions, we used an intermediate value of  $d=0.5$

$$G_5(M, R_{cl}) = \left[ (1 - (R_{cl}/R_3)^{0.5})^2 + 4D_3^2(R_{cl}/R_3)^{0.5} \right]^{-0.5} \quad (13)$$

where  $R_3 = c_{11}M^2 + c_{12}M + c_{13}$ , and  $R_3$  increases with magnitude. The values of  $c_{11}$ ,  $c_{12}$  and  $c_{13}$  are given in Figure 6. Use of  $G_5$  brings final attenuation at far distances to  $R^{-2.0}$ . For specific regions with certain Q-values, the coefficients in Eq. 12 can be further adjusted for regional fast or slow attenuation. We expect Q-values lower than 250 to correspond to fast attenuation, and Q-values of 400 and higher to correspond to slow attenuation. We would expect  $d(Q)$ -function to change from 0 to approximately 2.5 with  $d(Q)=0$  resulting in slow ( $R^{-1.5}$ ) and  $d(Q)=2.5$  in fast ( $R^{-4}$ ) attenuation depending upon Q-value.

### USGS - ATLAS GLOBAL DATABASE TEST

The above described modular approach and the GK-07 are examined here using the USGS - Atlas global database. In order to investigate the influence of magnitude scaling on attenuation of ground motion intensity, data is first categorized into 18 magnitude bins having an interval of 0.2, and then an average GK-07 attenuation curve (without basin effect) is compared with the corresponding data in each bin as shown in Figures 4 and 5. In these comparisons,  $V_{S30}$  of our predictions is taken as 400 m/sec as the average value of the dataset. These figures show that attenuation curve fits consistently well to actual data up to about 100 km from the source indicating that our core equation is a good approximation of ground motion attenuation for a range of magnitudes ( $4.2 \leq M \leq 7.9$ ).

In order to achieve a better fit to actual data, we modified a single parameter,  $R_0$  in our original equation. As defined earlier, this is a magnitude dependent corner distance parameter

between relatively flat attenuation and faster attenuation regions. As opposed to our initial  $R_0$  as shown in Figure 3 based on the NGA database, the Atlas database requires a slightly larger  $R_0$  value. Our new  $c_4$  and  $c_5$  parameters defining  $R_0$  were computed as 3.67 and -12.42, respectively. To enhance far distance predictions ( $>100$  km) where generally faster attenuation is observed, we utilized the  $G_5$  filter (defined in previous section). The GMPE with modified  $R_0$  and far distance attenuation filter is called here as “GK-09”. The GK-09 with its estimator coefficients is described in Figure 6. The predictive power of the GK-09 is compared with the GK-07 and also with the actual recorded ground motion data in Figures 4 and 5. Note that the GK-07 and GK-09 behave almost same at  $R_{cl} \leq 100$  km, the difference (slightly higher prediction due to the GK-07 at near-field, and opposite at far-field) is associated with the first term added to the  $G_5$  filter, which is  $c_{10}$ , without this scaling term the GK-07 and GK-09 would produce exactly the same results at  $R_{cl} \leq 100$  km. This scaling term is required to avoid distance bias in predictions (discussed further later). From the comparisons, it is evident that the  $G_5$  filter in the GK-09 leads to visually enhanced fit to data both at near- and far-field. Distribution of residuals with magnitude, distance and  $V_{S30}$  shown in Figure 8 confirms this conclusion (discussed in more detail in the next section).

The performance of the GK-09 is further demonstrated against the most damaging recent earthquakes in Figure 9 where our predictions are compared with strong motion data from the 2008 M7.9 Wenchuan (China) and 2009 *M*6.3 L’Aquilla (Italy) earthquakes. The GK-09 curves are computed for the average shear-wave velocities in each dataset. At far-field, the Wenchuan earthquake data demonstrate slow attenuation; as opposed to fast attenuation of data from the 2009 *M*6.3 L’Aquilla, Italy earthquake. For both events, the GK-09 produces good predictions.

## RESIDUAL ANALYSIS AND STANDARD ERROR

We computed the standard error ( $\sigma$ ) of prediction according to following equation:

$$\sigma = \left[ \sum (x_i - x'_i)^2 / (n - p) \right]^{0.5} \quad (14)$$

where  $x_i$  denotes the  $i^{th}$  value of observation and  $x'_i$  is its prediction.  $(x_i - x'_i)$  is the residual of the  $i^{th}$  observation, and  $p$  is the number of dependent parameters of estimation.  $\sigma$  of the original GK-07 relation based on the NGA database is computed as 0.55. Fitting GK-07 and GK-09 to the Atlas database yields  $\sigma$  as 0.85 and 0.83, respectively. Thus, the grey zones indicated in Figures 4 and 5 bounded by 16- and 84 percentile ( $\pm \sigma$ ) of the predictions are practically valid for both GMPEs. As evident, most of the data falling within this grey zone indicates reasonable

predictions due to both GMPEs. Although, Eq. (14) implies that  $\sigma$  has the tendency to reduce when number of data points ( $n$ ) increases, the opposite takes place because the variability in ground motion intensity increases with increase in database size.

In addition to the total  $\sigma$  based on the entire database, it is also instructive to explore the variation of  $\sigma$  within each magnitude bin. This will give us an idea about the stability of the GMPE in predicting ground motion at different magnitude levels.  $\sigma$  due to the GK-07 and GK-09 are marked in each panel in Figures 4 and 5; these values are plotted in Figure 7a to check for dependence of  $\sigma$  against magnitude. As shown,  $\sigma$  demonstrates very low dependence on magnitude. This observed dependence demonstrates a similar trend as shown in Strasser et al. (2009) but with a much lower slope. We also investigated dependence of  $\sigma$  on distance. Similar to the magnitude bins, we created distance bins with an interval of 20 km, and computed  $\sigma$  for the group of data falling into each distance bin. Figure 7b plots the variation of  $\sigma$  with respect to twenty-five distance bins.  $\sigma$  demonstrates relatively low dependence on distance; it decreases with increase in distance.

There are two main approaches in modeling  $\sigma$ : constant (e.g., Boore and Atkinson, 2008; Campbell and Bozorgnia, 2008) and magnitude dependent (e.g., Abrahamson and Silva, 2008; Chiou and Youngs, 2008). Wang (2009) states that  $\sigma$  is actually depending upon magnitude and distance. Based on the results shown in Figure 7a and 7b it is possible to consider  $\sigma$  to be magnitude and distance dependent using the following linear relations:

$$\begin{aligned}\sigma(M) &= -0.043M + 1.10 \\ \sigma(R_{cl}) &= -0.0004R_{cl} + 0.89\end{aligned}\tag{15}$$

In order to investigate whether our predictions are biased against any independent parameters of estimations, residuals of predictions against magnitude, fault distance and  $V_{S30}$  are plotted in Figure 8. The GK-07 shows a slight distance bias at far-field (over prediction), and no bias with respect to magnitude and style of faulting. Note that the GK-07 is developed using data up to 200 km; the over prediction trend at far distances over 200 km is due to faster attenuation of low-amplitude data (such data is missing in the NGA database). Using an additional  $G_5$  filter, we were able to eliminate this far-field distance bias in the GK-09. Similar to the GK-07, GK-09 does not show any bias with respect to magnitude and style of faulting. These results indicate that GK-09 can be reliably used for global ground motion predictions.

## CONCLUSIONS

In this paper, we tested the GK-07 and its modular approach using the part of global Atlas dataset representing worldwide shallow crustal regions. We observed that for distances more than 100 km from the fault, attenuation of ground motion demonstrates two main tendencies: fast attenuation in the order of  $R^{-4}$ , and slow attenuation in the order of  $R^{-1.5}$ . For regions similar to the Central and Eastern U.S. with relatively high Q-values ground motion attenuation is about  $R^{-1.5}$  at the near- and far-field, whereas for the Western U.S. with relatively low Q-values attenuation slope for distances of approximately more than 100 km is higher (almost  $R^{-4}$ ).

We used a total of 13,992 records from 244 crustal earthquakes. The current set includes data recorded within 500 km of the earthquake source from events in the magnitude range from 4.2 to 7.9. With a calibration of two estimator coefficients in our original equation (GK-07) and implementing an additional far distance filter ( $G_5$ ), we were able to obtain strong correlation between recorded data and predicted ones up to about 500 km from the fault. There is no bias observed against distance, magnitude and  $V_{S30}$  measures. This demonstrates the potential use of the GK-09 in predicting ground motions from shallow crustal regions. Standard error of the original GK-07 is 0.55 based on about 2000 data points; fitting the GK-09 to the Atlas database, which has seven times more data points, yields a standard error of 0.83. Increase in standard error is expected since the variability in ground motions escalates with increase in database size. We found relatively weak dependence of standard error to magnitude and distance; the standard error tends to decrease with the increase in  $M$  and  $R_{cl}$ .

The modular modeling approach in ground motion prediction as presented for shallow crustal regions here can be used for other tectonic regions where subduction and intraplate events dominate the hazard. We expect a number of developed modules including the core filter  $G_2$ , the basin effect filter  $G_3$ , and the site correction filter  $G_4$  to be applicable for different environments.

For calculation of spectral acceleration (SA) response values, the GK-09 presented herein can be used together with our PGA-based predictive model for SA as described in Graizer and Kalkan (2009). Comparison of the GK-09 with the recent NGA models is currently underway.

## ACKNOWLEDGMENTS

We thank Dave Wald for his suggestions, and Prof. Izzat M. Idriss for providing results of his 2009 SSA presentation. Sincere thanks are extended to Shojiro Kataoka and Chris Stephens for reviewing this article. We also like to thank China Strong Motion Networks Center (CSMNC)

for generously providing us the Wenchuan Earthquake data, and Antoine Le Metayer for his help on this dataset.

The GK-07 and GK-09 ground motion prediction equations were coded in FORTRAN, M.S. Excel and MatLAB, and their source codes are available upon request. Any opinions, findings, and conclusions or recommendations expressed in this paper are those of the authors solely and do not necessarily reflect the views of the U.S. Nuclear Regulatory Commission.

## REFERENCES

- Abrahamson, N.A. and Silva, W.J. (2008). Summary of the Abrahamson and Silva NGA ground motion relations, *Earthquake Spectra*, **24**, No. 1, 67-98.
- Boore, D. M., Joyner, W. B., and Fumal, T. E., 1997. Equations for estimating horizontal response spectra and peak acceleration from western North American earthquakes: a summary of recent work. *Seismol. Res. Lett.* **68**, 128-153.
- Boore, D. M., and Atkinson, G. M., 2008. Ground motion prediction equations for the average horizontal component of PGA, PGV, and 5%-damped PSA at spectral periods between 0.01 s and 10.0 s, *Earthquake Spectra*, **24**, No. 1, 99-138.
- Brune, J. (1970). Tectonic stress and the spectra of seismic shear waves from earthquakes. *J. Geophys. Res.*, **75**, 4997-5009.
- Brune, J. (1971). Correction. *J. Geophys. Res.*, **76**, 5002.
- Burger, R. w., P. G. Somerville, J. S. Barker, R. B. Herrmann, and D. V. Helmberger (1987). The effect of crustal structure on strong ground motion attenuation relations in eastern North America, *Bull. Seismol. Soc. Am.* **77**, 420–439.
- Campbell, K. W., 1997. Empirical near-source attenuation relationships for horizontal and vertical components of peak ground acceleration, peak ground velocity, and pseudo-absolute acceleration response spectra. *Seismol. Res. Lett.* **68**, 154-179.
- Campbell, K. W., 2003. Strong-motion attenuation relations, in *International Handbook of Earthquake and Engineering Seismology, Part B*, edited by W. H. K. Lee, H. Kanamori, P. C. Jennings, and C. Kisslinger, Academic Press, Burlington, Mass., 1003–1012.
- Campbell, K. W., and Bozorgnia, Y., 2008. NGA ground motion model for the geometric mean horizontal component of PGA, PGV, PGD and 5% damped linear elastic response spectra for periods ranging from 0.01 to 10 s, *Earthquake Spectra*, **24**, No. 1, 139-172.

- Chandler, A.M. N.T.K. Lam and H.H. Tsang (2006). Near-surface attenuation modelling based on rock shear-wave velocity profile. *Soil Dynamics and Earthquake Engineering*, **26**, No. 11, 1004-1014.
- Chinnery, M. A., 1961. The deformation of the ground around surface faults, *Bull. Seismol. Soc. Am.* **51**, 355–372.
- Chiou, B., and Youngs, R., 2008. An NGA model for the average horizontal component of peak ground motion and response spectra, *Earthquake Spectra*, **24**, No. 1, 173-216.
- Choi, Y., and Stewart, J. P., 2005. Nonlinear site amplification as a function of 30 m shear wave velocity. *Earthquake Spectra*, **21**, No.1, p.1-30.
- Field, E. H., 2000. A modified ground motion attenuation relationship for Southern California that accounts for detailed site classification and a basin-depth effect. *Bull. Seism. Soc. Amer.*, **90**, 209-221.
- Frankel, A., Carver, D., Cranswick, E., Bice, T., Sell, R., and Hanson, S., 2001. Observation of basin ground motions from a dense seismic array in San Jose, California. *Bull. Seism. Soc. Am.*, **91**, 1-12.
- Graizer, V. and Kalkan, E., 2007. Ground Motion Attenuation Model for Peak Horizontal Acceleration from Shallow Crustal Earthquakes, *Earthquake Spectra*, **23**, No. 3, 585-613.
- Graizer, V. and Kalkan, E., 2009. Prediction of response spectral acceleration ordinates based on PGA attenuation, *Earthquake Spectra*, **25**, No. 1, 39-69.
- Haskell, N. A., 1969. Elastic displacements in the near-field of a propagating fault, *Bull. Seismol. Soc. Am.* **59**, 865–908.
- Idriss, I.M. (2008). An NGA empirical model for estimating the horizontal spectral values generated by shallow crustal earthquakes, *Earthquake Spectra*, **24**, (in press).
- Lee, V. W., Trifunac, M. D., Todorovska, M. I. and Novikova, E. I., 1995. Empirical equations describing attenuation of peak of strong ground motion, in terms of magnitude, distance, path effects and site conditions. Report No. CE 95-02. Los Angeles, California. 268 p.
- Liu, K. S. and Tsai Y. B. (2009). Large effects of Moho reflections (*SmS*) on peak ground motion in Northwestern Taiwan. *Bull. Seismol. Soc. Am.*, **99**, 255-267.
- Mitchell, B. J., and H. J. Hwang (1987). Effect of low Q sediments and crustal Q on Lg attenuation in the United States. *Bull. Seism. Soc. America*, **77**, No. 4, 1197-1210.
- Singh, S. and R. B. Herrmann (1983). Regionalization of crustal coda Q in the continental United States, *J. Geophys. Res.*, **88**, 527-538.

Somerville, P. G., and J. Yoshimura (1990). The influence of critical Moho reflections on strong ground motions recorded in San Francisco and Oakland and during the 1989 Loma Prieta earthquake, *Geophys. Res. Lett.*, **17**, 1203–1206.

Strasser F.O., Abrahamson N.E., and J.J. Bommer (2009). Sigma: Issues, Insights, and Challenges. *Seism. Res. Letters*, **80**, No.1, pp. 40-56.

Wang, Z., (2009). Comment on "Sigma: Issues, Insights, and Challenges" by F. O. Strasser, N. A. Abrahamson, and J. J. Bommer. *Seismol. Res. Lett.* **80**, 491-493.

Appendix – A1. List of events utilized in the USGS - Global Atlas ground motion database

No.	Location	Mw	Num. of Data	Style of Faulting	No.	Location	Mw	Num. of Data	Style of Faulting
1	Adana-Ceyhan, Turkey	6.3	9	Strike-Slip	53	Elmore Ranch, California	6	1	Strike-Slip
2	Altinsac, Turkey	5.5	1	Reverse	54	Epagny, France	4.3	3	Undefined
3	Anchialos, Greece	5.6	2	Normal	55	Erzincan, Turkey	6.6	3	Strike-Slip
4	Anza	5.2	101	Strike-Slip	56	Eureka, California	7	2	Strike-Slip
5	Anza, California	5.6	3	Undefined	57	Faial Island, Portugal	6.1	5	Strike-Slip
6	Ardakul, Iran	7.2	1	Strike-Slip	58	Filippias, Greece	5.5	5	Reverse
7	Ardebil, Iran	6.1	19	Strike-Slip	59	Fiordland, New Zealand	5.8	10	Reverse
8	Arthurs Pass, New Zealand	6.7	18	Strike-Slip	60	Firuzabad, Iran	5.9	9	Strike-Slip
9	Athens, Greece	6	1	Normal	61	Friuli, Italy	6.5	22	Reverse
10	Azores, Portugal	5.9	4	Strike-Slip	62	Friuli, Italy (Aftershock)	5.9	18	Undefined
11	Baiano, Italy	4.9	2	Undefined	63	Friuli, Italy (Foreshock)	5.5	15	Undefined
12	Baja California, Mexico	5.1	36	Strike-Slip	64	Fukuoka, Japan	6.6	271	Strike-Slip
13	Baja California, Mexico (Aftershock)	5	23	Undefined	65	Garmkhan, Iran	6.5	10	Strike-Slip
14	Bam, Iran	6.6	1	Strike-Slip	66	Gazli, Uzbekistan	6.7	1	Reverse
15	Banja Luka, Bosnia and Herzegovina	5.7	4	Strike-Slip	67	Geiyo, Japan	6.8	316	Normal
16	Basilicata, Italy	5.2	1	Undefined	68	Gisborne, New Zealand	5.6	4	Undefined
17	Bhuj, India (Aftershock)	5.3	1	Undefined	69	Godley River, New Zealand	6.1	1	Strike-Slip
18	Big Bear City	5.2	91	Strike-Slip	70	Golbaf, Iran	6.6	5	Strike-Slip
19	Big Bear, California	6.5	26	Strike-Slip	71	Golbasi, Turkey	6	3	Strike-Slip
20	Biga, Turkey	6.1	5	Strike-Slip	72	Golcayir, Turkey	6	1	Normal
21	Bingol, Turkey	6.3	4	Strike-Slip	73	Griva, Greece	6.1	6	Normal
22	Bitola, Macedonia	5.6	2	Undefined	74	Guerrero, Mexico	6.9	151	Reverse
23	Boolarra, Australia	4.2	14	Undefined	75	Gulf of Akaba, Saudi Arabia	7.2	7	Strike-Slip
24	Borrego Mountain, California	6.6	1	Strike-Slip	76	Gulf of Akaba, Saudi Arabia (Aftershock)	5.7	1	Strike-Slip
25	Boumerdes, Algeria	6.8	13	Reverse	77	Gulf of California, Mexico	5.7	2	Strike-Slip
26	Bovec, Slovenia	5.6	13	Strike-Slip	78	Haciavililer, Turkey	4.8	2	Undefined
27	Brijezde, Serbia	5.5	1	Strike-Slip	79	Hastings, New Zealand	5.6	1	Normal
28	Calabria, Italy	5.2	2	Normal	80	Hawks Bay, New Zealand	5.4	2	Normal
29	Cape Campbell, New Zealand	6.1	30	Normal	81	Hawks Crag, New Zealand	5.8	22	Reverse
30	Cass, New Zealand	6.1	11	Strike-Slip	82	Hector Mine, California	7.1	105	Strike-Slip
31	Chahar Mahal Bakhtiari, Iran	6	1	Strike-Slip	83	Hector Mine, California (Aftershock)	5.7	69	Undefined
32	Chalfant Valley, California	6.2	6	Strike-Slip	84	Hendek-Akyazi, Turkey	5.3	8	Strike-Slip
33	Chalfant Valley, California (After)	5.7	5	Reverse	85	Hokkaido, Japan	7	356	Reverse
34	Chalfant Valley, California (Fore)	5.8	4	Normal	86	Hokkaido, Japan (Aftershock)	6.7	355	Reverse
35	Chamoli, India	6.5	11	Reverse	87	Honeydew, California	6.1	4	Reverse
36	Changureh-Avaj, Iran	6.5	62	Reverse	88	Honshu, Japan	6.6	2416	Reverse
37	Charles Sound, New Zealand	6.1	1	Reverse	89	Horasan-Narman, Turkey	6.6	1	Strike-Slip
38	Chenoua, Algeria	5.9	3	Reverse	90	Hualien, Taiwan	6.2	36	Reverse
39	Chi-Chi, Taiwan	7.7	407	Reverse	91	Hyuga-Nada #2, Japan	6.7	121	Reverse
40	Chi-Chi, Taiwan (Aftershock)	6.6	1096	Reverse	92	Ibaraki Prefecture, Japan	5.4	199	Reverse
41	Chino Hills, California	5.4	462	Undefined	93	Imotski-Grude, Croatia	5.6	1	Undefined
42	Chios, Greece	5.6	2	Strike-Slip	94	Imperial Valley, California	6.5	38	Strike-Slip
43	Coalinga, California	6.3	53	Reverse	95	Inangahua, New Zealand	7.2	15	Undefined
44	Coalinga, California (Aftershock)	5.1	7	Reverse	96	India-Bangladesh Border	5.8	18	Strike-Slip
45	Coast of Guerrero, Mexico	5.8	4	Reverse	97	India-Burma Border	7.2	33	Reverse
46	Coast of Northern California	7.2	8	Strike-Slip	98	India-Burma Border	5.9	11	Strike-Slip
47	Corinth, Greece	6.6	2	Normal	99	Ionian, Greece	5.4	1	Undefined
48	Corinth, Greece (Aftershock)	6.3	1	Normal	100	Irpinia, Italy	6.9	1	Normal
49	Cosenza, Italy	4.8	1	Undefined	101	Ishakli, Turkey	6.5	7	Normal
50	Coyote Lake, California	5.7	2	Strike-Slip	102	Ishakli, Turkey (Aftershock)	5.8	5	Normal
51	Cyprus	6.8	1	Strike-Slip	103	Itea, Greece	5.6	4	Normal
52	Dahuiyeh, Iran	6.4	21	Reverse	104	Iwate, Japan	6.9	395	Undefined
53	Dead Sea, Israel	5.1	3	Strike-Slip	105	Izmir, Turkey	6	5	Strike-Slip
54	Denali, Alaska	7.9	24	Strike-Slip	106	Joshua Tree, California	6.2	1	Strike-Slip
55	Dharmasala, India	5.5	9	Reverse	107	Kagoshima, Japan	6.1	26	Strike-Slip
56	Dillon, Montana	5.6	7	Normal	108	Kagoshimaen-Hoku-Seibu, Japan	6	22	Strike-Slip
57	Dinar, Turkey	6.4	7	Normal	109	Kalamata, Greece	6.4	8	Strike-Slip
58	Doubtful Sound, New Zealand	6.4	2	Reverse	110	Kalamata, Greece (Aftershock)	4.8	3	Undefined
59	Duzce, Turkey	7.1	1	Strike-Slip	111	Kallirro, Greece	5.4	1	Normal
60	Duzce, Turkey (Aftershock)	6	3	Reverse	112	Karebas, Iran	6.2	19	Strike-Slip
61	East Cape, New Zealand	7.1	15	Normal	113	Kefallinia Island, Greece	6.9	7	Strike-Slip
62	Edgcombe, New Zealand	6.5	2	Normal	114	Kefallinia Island, Greece (Aftershock)	6.2	3	Strike-Slip
63	Edgcombe, New Zealand (After)	5.8	1	Undefined	115	Kiholo Bay, Hawaii	6.7	23	Normal
64	Ellalong, Australia	4.7	9	Undefined	116	Kiholo Bay, Hawaii (Aftershock)	6	18	Reverse

## Appendix – A1. (cont')

No.	Location	Mw	Num. of Data	Style of Faulting	No.	Location	Mw	Num. of Data	Style of Faulting
117	Kobe, Japan	6.9	23	Strike-Slip	181	Reggio nell'Emilia, Italy	5.2	2	Undefined
118	Kocaeli, Turkey	7.6	38	Strike-Slip	182	Rotorua, New Zealand	5.4	8	Strike-Slip
119	Kocaeli, Turkey (Aftershock)	5.8	76	Strike-Slip	183	Ryukyu Islands, Japan	5.7	3	Reverse
120	Kojur-Firoozabad, Iran	6.3	100	Reverse	184	Saguenay, Canada	5.8	2	Reverse
121	Kopaonik, Serbia	5.9	2	Strike-Slip	185	Sahneh, Iran	5.2	5	Reverse
122	Koyyeri, Turkey	5.2	1	Undefined	186	Saint Die, France	5	8	Normal
123	Kozani-Grevena, Greece	6.6	10	Normal	187	Salehabad, Iran	5.5	3	Reverse
124	Kyllini, Greece	5.9	6	Strike-Slip	188	San Fernando, California	6.6	111	Undefined
125	Kyushu, Japan	6.4	77	Reverse	189	San Juan Bautista, California	5.2	2	Strike-Slip
126	Lake Tahoe, Nevada	5.9	1	Strike-Slip	190	San Simeon	6.5	51	Reverse
127	Lake Tennyson, New Zealand	6	3	Strike-Slip	191	Santa Barbara, California	5.8	3	Reverse
128	Landers, California	7.3	44	Strike-Slip	192	Sapanca-Adapazari, Turkey	5.6	25	Strike-Slip
129	L'Aquila	6.3	55	Normal	193	Sarria Becerreá, Spain	4.9	1	Undefined
130	Lazio Abruzzo, Italy	5.9	15	Normal	194	Satsop, Washington	5.8	4	Normal
131	Lazio Abruzzo, Italy (Aftershock)	5.5	9	Normal	195	Sea of Japan	5.9	22	Reverse
132	Livermore, California	5.8	9	Reverse	196	Secretary Island, New Zealand	6.9	5	Reverse
133	Loma Prieta, California	6.9	34	Reverse	197	Seferihisar, Turkey	5.7	9	Strike-Slip
134	Lytle Creek, California	5.4	1	Undefined	198	Shikoku, Japan	5.7	138	Strike-Slip
135	Magon Oros Peninsula, Greece	6.6	3	Strike-Slip	199	Sicily, Italy	5.8	7	Strike-Slip
136	Mammoth Lakes, California	5.9	1	Normal	200	Sierra Madre, California	5.6	1	Reverse
137	Managua, Nicaragua	6.2	1	Undefined	201	Southern Honshu, Japan	5.5	181	Reverse
138	Manjil, Iran	7.4	1	Strike-Slip	202	Spitak, Armenia	6.7	1	Reverse
139	Masjed-E-Soleyman, Iran	5.6	3	Reverse	203	Strofades, Greece	6.6	10	Reverse
140	Meckering, Australia	4.2	1	Undefined	204	Superstition Hills, California	6.5	4	Strike-Slip
141	Meydan, Turkey	5.4	5	Normal	205	Sur, Lebanon	5.6	1	Undefined
142	Michoacan, Mexico	7.1	36	Strike-Slip	206	Tabas, Iran	7.3	1	Reverse
143	Milford Sound, New Zealand	6.5	3	Reverse	207	Tadmuriyah, Syria	5.5	10	Strike-Slip
144	Milpitas, California	5.6	211	Strike-Slip	208	Taiwan	6.4	96	Strike-Slip
145	Miyagi-Hokubu, Japan	6	199	Reverse	209	Tangshan, China	7.6	6	Strike-Slip
146	Miyagi-Oki, Japan	7	364	Reverse	210	Tbilisi, Georgia	4.8	1	Undefined
147	Montenegro, Serbia	6.9	20	Reverse	211	Te Anau, New Zealand	6.7	2	Strike-Slip
148	Montenegro, Serbia (Aftershock)	6.2	14	Reverse	212	Te Kuha, New Zealand	6.3	7	Strike-Slip
149	Morgan Hill, California	6.2	9	Strike-Slip	213	Terceira Island, Portugal	6.9	1	Strike-Slip
150	Mt. Carmel, Illinois	5.2	11	Undefined	214	Thessaloniki, Greece	6.2	1	Normal
151	Mt. Carmel, Illinois (Aftershock)	4.6	2	Undefined	215	Thomson Reservoir, Australia	4.5	15	Undefined
152	Muradiye, Turkey	7	1	Strike-Slip	216	Tikokino, New Zealand	5.7	10	Reverse
153	New Zealand	6.2	11	Strike-Slip	217	Tirana, Albania	5.9	2	Reverse
154	Niigata, Japan	6.6	1	Reverse	218	Tithorea, Greece	5.9	4	Normal
155	Niigata, Japan (Aftershock)	6.3	1684	Reverse	219	Tokachi-Oki, Japan (Aftershock)	6.7	79	Reverse
156	Nisqually, Washington	6.8	62	Normal	220	Tokomaru, New Zealand	5.7	2	Reverse
157	North Palm Springs, California	6	11	Reverse	221	Tottori, Japan	6.7	303	Strike-Slip
158	Northridge, California	6.7	71	Reverse	222	Trinidad, California	7.3	1	Strike-Slip
159	Northwest China	6.1	8	Normal	223	Turkmenistan	7	12	Reverse
160	Noto Peninsula, Japan	6.7	377	Undefined	224	Umbria-Marche, Italy	6	26	Normal
161	Oaxaca, Mexico	7.1	3	Reverse	225	Umbria-Marche, Italy (Aftershock)	5.9	49	Strike-Slip
162	Obsidian Butte, California	5.2	44	Strike-Slip	226	Umbria-Marche, Italy (Foreshock)	5.7	19	Normal
163	Off coast of Karpathos, Greece	6.2	1	Strike-Slip	227	Upland, California	5.7	1	Strike-Slip
164	Ormond, New Zealand	6.4	24	Strike-Slip	228	Urmia, Iran	5.8	1	Normal
165	Parkfield, California	6.1	232	Strike-Slip	229	Valnerina, Italy	5.8	7	Normal
166	Parma, Italy	5	1	Reverse	230	Valparaíso, Chile (Aftershock)	7	1	Undefined
167	Pasinler, Turkey	5.4	1	Strike-Slip	231	Victoria, Mexico	6.3	6	Strike-Slip
168	Patras, Greece	5.6	10	Strike-Slip	232	Volos, Greece	6.6	1	Normal
169	Peru	6.6	2	Undefined	233	Volos, Greece (Aftershock)	6.3	1	Undefined
170	Petrolia, California	7.2	7	Reverse	234	Vrancea, Romania	7.5	23	Reverse
171	Petrolia, California (Aftershock)	6.6	8	Strike-Slip	235	Weber, New Zealand	6.4	54	Strike-Slip
172	Pol-e-Abgineh, Iran	5.2	6	Reverse	236	Wells, Nevada	6	69	Normal
173	Polkowice, Poland	5	1	Undefined	237	Wenchuan, China	7.9	32	Undefined
174	Potenza, Italy	5.8	3	Strike-Slip	238	West of Invercargill, New Zealand	7.1	12	Reverse
175	Preveza, Greece	5.4	4	Reverse	239	Western Honshu, Japan	5.1	197	Reverse
176	Puebla, Mexico	6.9	15	Normal	240	Whittier Narrows, California	5.9	24	Reverse
177	Pulumur, Turkey	6	5	Strike-Slip	241	Whittier Narrows, California (After)	5.2	3	Strike-Slip
178	Pyrgos, Greece	5.4	2	Strike-Slip	242	Yamaguchi, Japan	5.8	174	Strike-Slip
179	Racha, Georgia	7	6	Reverse	243	Yountville, California	5	27	Undefined
180	Racha, Georgia (Aftershock)	6.2	12	Reverse	244	Yucaipa	4.9	187	Reverse

## Figure Captions

**Figure 1.** Distribution of PGA values with respect to moment magnitude ( $M_w$ ), closest fault distance ( $R_{cl}$ ), shear-wave velocity ( $V_{S30}$ ), and style of faulting [UnDef = Undefined; Rev = Reverse; S-Slip = Strike-slip; Norm= Normal faulting]; See Appendix –A1 for complementary information.

**Figure 2.** [a] 2004  $M_w$  6.0 Parkfield earthquake PGA data and approximation curves for ground motion attenuation (low amplitude data show fast attenuation); [b] examples of filters modeling different physical phenomena: core attenuation, basin, and far-distance-fast attenuation; [c] effects of basin filter and far-distance fast attenuation filter on core attenuation curve; [d] modeling Moho reflection.

**Figure 3.** GK-07 attenuation relation for free-field horizontal component of ground motion (Graizer and Kalkan, 2007).

**Figure 4.** Comparison of GK-07 and GK-09 GMPEs with the USGS - ATLAS database for  $4.2 \leq M_w \leq 6.2$ ; data is divided into magnitude bins with an interval of 0.2; grey zones are bounded by  $\pm\sigma$  of predictions.

**Figure 5.** Comparison of GK-07 and GK-09 GMPEs with the USGS - ATLAS database for  $6.2 \leq M_w \leq 8.0$ ; data is divided into magnitude bins with an interval of 0.2.

**Figure 6.** GK-09 global attenuation relation for free-field horizontal component of ground motion.

**Figure 7.** Variation of  $\sigma_{lnY}$  (standard error of prediction) with respect to magnitude,  $M_w$  [left] and closest fault distance,  $R_{cl}$  [right] Ground motion data is binned based on magnitude interval of 0.2 and distance interval of 20 km.

**Figure 8.** Distribution of residuals with respect to closest fault distance ( $R_{cl}$ ), magnitude ( $M_w$ ) and shear-wave velocity ( $V_{S30}$ ) for GK-07 [top row]; and for GK-09 [bottom row].

**Figure 9.** Ground motion predictions from GK-09 for the  $M_w$ 6.3 Central Italy L'Aquila earthquake [left], and for the  $M_w$ 7.9 Wenchuan, China earthquake [right]; data show slow attenuation for Wenchuan as opposed to fast attenuation for L'Aquila. (GK-09 predictions are based on average  $V_{S30}$  of each data set).

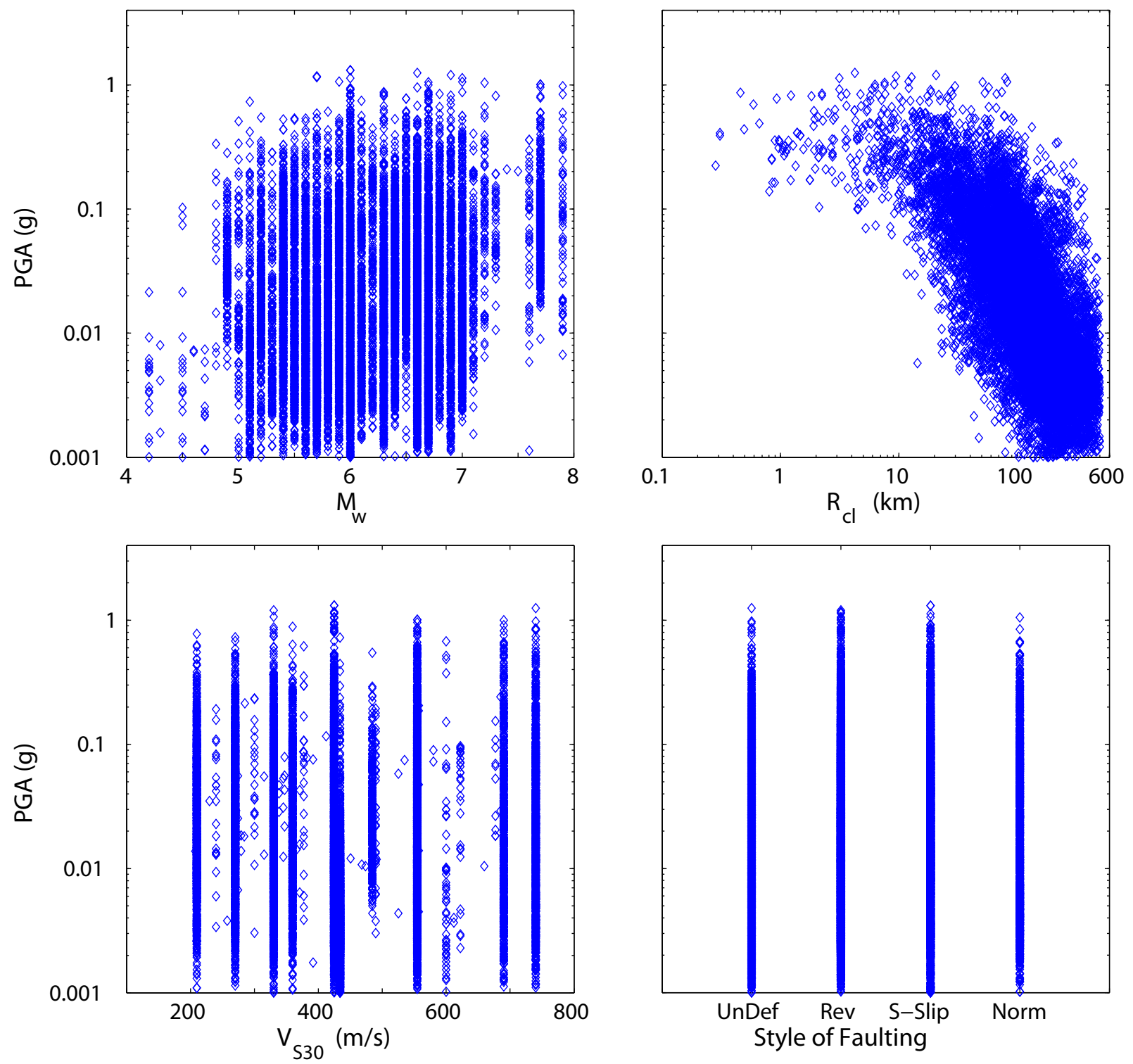


**Figure 1**

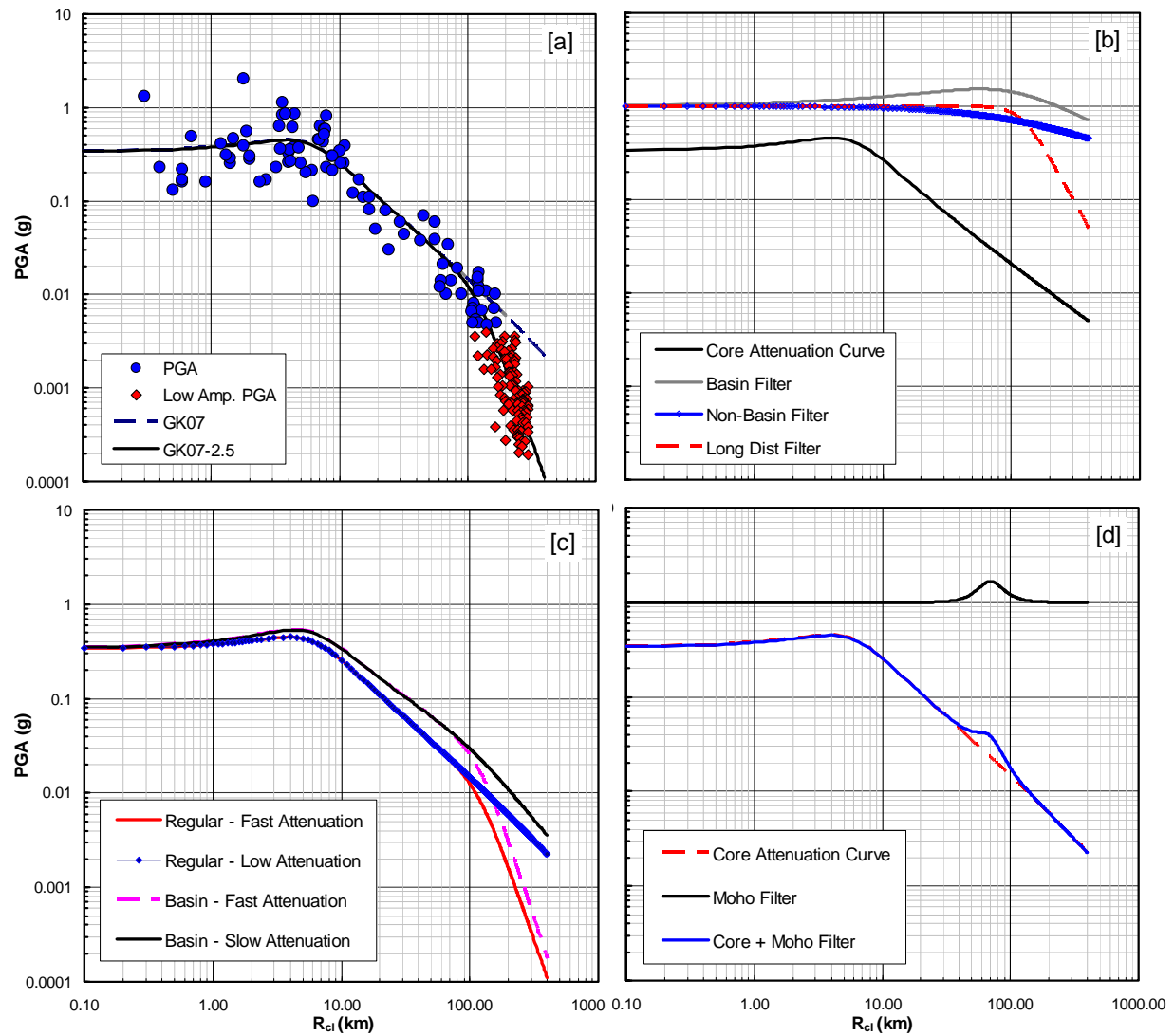


**Figure 2**



$$PGA = G_1 \times G_2 \times G_3 \times G_4$$

**G<sub>1</sub>** = Magnitude and Style of Faulting Scaling    **X**  
**G<sub>2</sub>** = Core Attenuation Equation    **X**  
**G<sub>3</sub>** = Basin Effect and Far Distance Correction    **X**  
**G<sub>4</sub>** = Site Correction

$$\ln(PGA) = \underbrace{\ln[A(M, F)]}_{G_1} - \underbrace{0.5\ln[(1-r_0)^2 + 4D_0^2r_0]}_{G_2} - \underbrace{0.5\ln[(1-\sqrt{r_1})^2 + 4D_1^2\sqrt{r_1}]}_{G_3} + b_v \ln(V_{S30}/VA) + \sigma_{\ln(PGA)}$$

where

$$r_0 = R_{cl} / R_0 \quad r_1 = R_{cl} / R_1$$

$$A(M, F) = [c_1 \arctan(M + c_2) + c_3] F$$

$$R_0 = c_4 M + c_5$$

$$D_0 = c_6 \cos[c_7(M + c_8)] + c_9$$

<b>c<sub>1</sub></b>	<b>c<sub>2</sub></b>	<b>c<sub>3</sub></b>	<b>c<sub>4</sub></b>	<b>c<sub>5</sub></b>	<b>c<sub>6</sub></b>	<b>c<sub>7</sub></b>	<b>c<sub>8</sub></b>	<b>C<sub>9</sub></b>	<b>b<sub>v</sub></b>	<b>VA</b>	<b>R<sub>I</sub></b>	<b>σ<sub>ln(PGA)</sub></b>
0.14	-6.25	0.37	2.237	-7.542	-0.125	1.19	-6.15	0.525	-0.24	484.5	100	0.552

**Note (1):** To capture basin effect it is recommended to set  $D_L = 0.35$ , otherwise  $D_L = 0.65$

(2):  $F = 1.00$  for strike-slip and normal faulting;  $F = 1.28$  for reverse faulting

(3):  $R_{cl}$  = Closest fault distance and  $M$  = Moment magnitude

**Figure 3.**

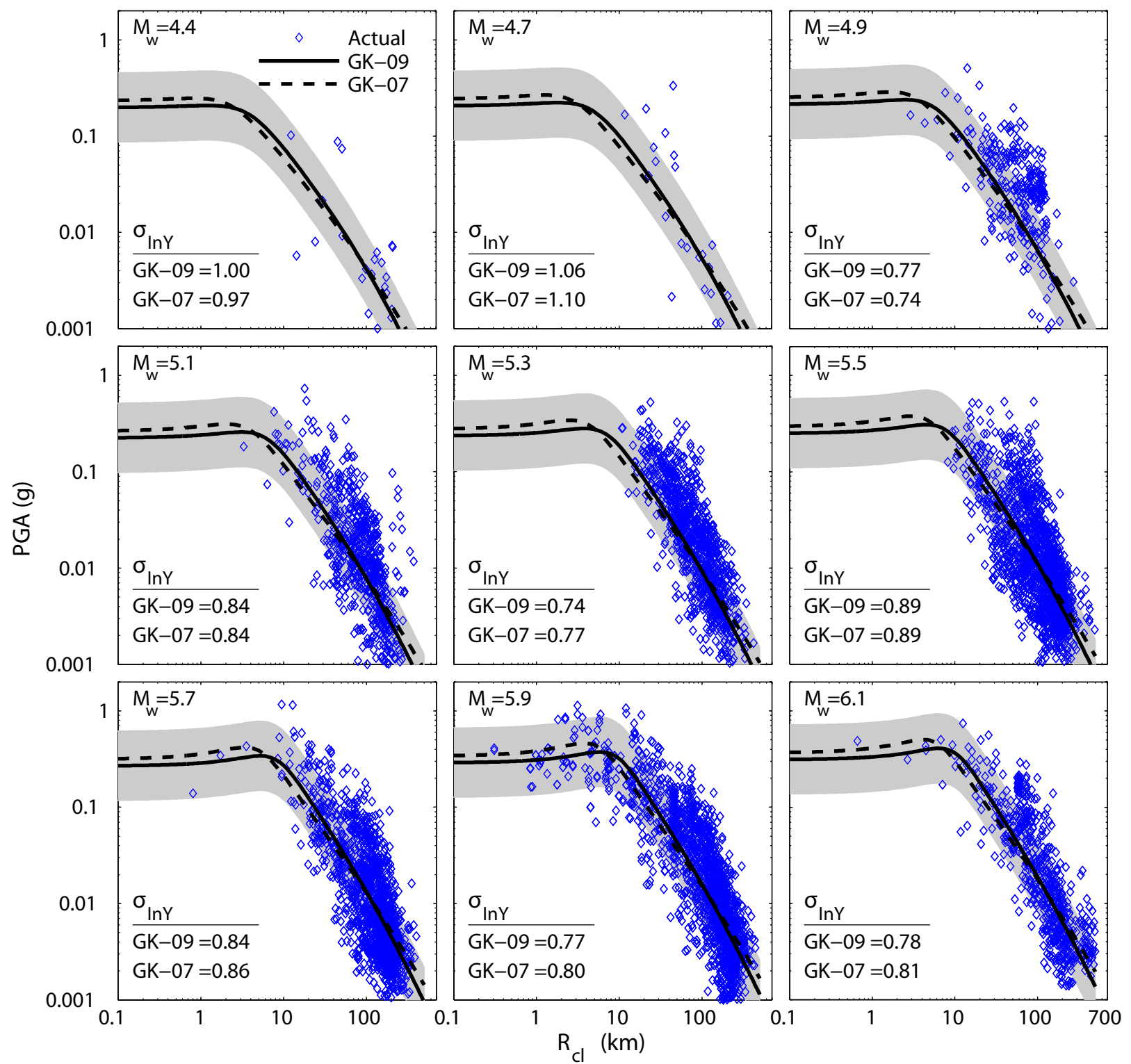
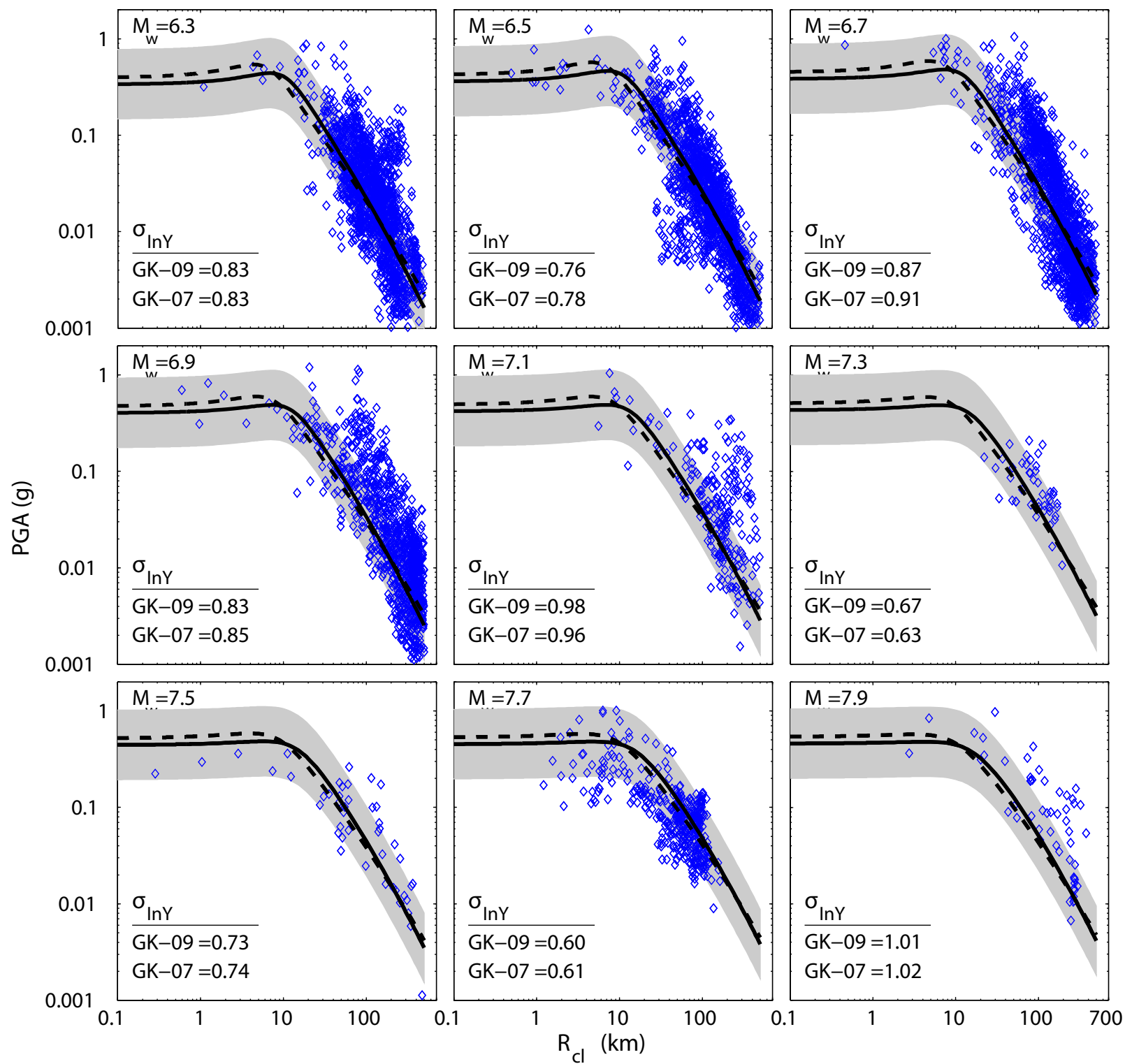
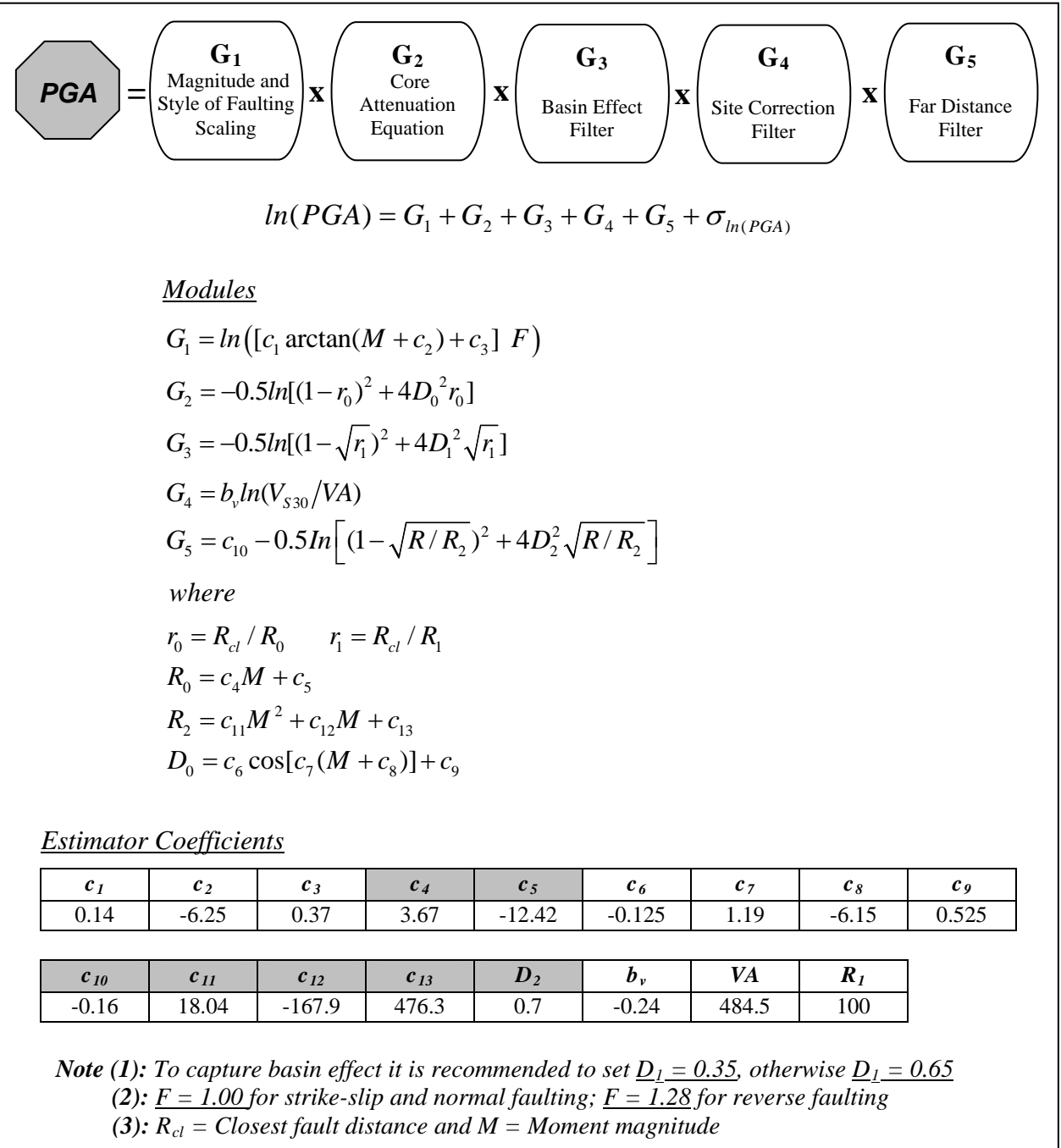


Figure 4



**Figure 5**



**Figure 6.**

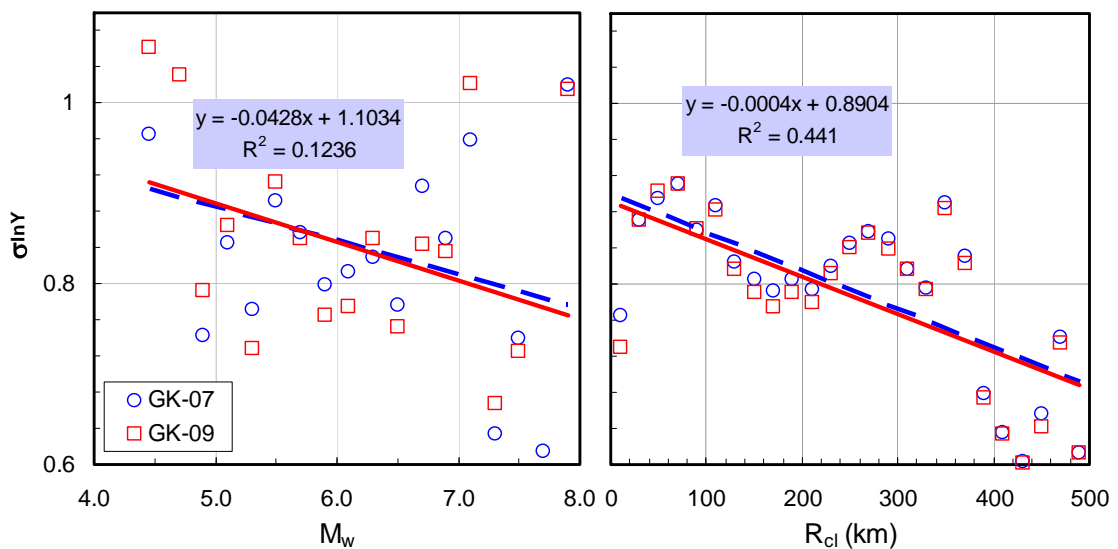


**Figure 7.**

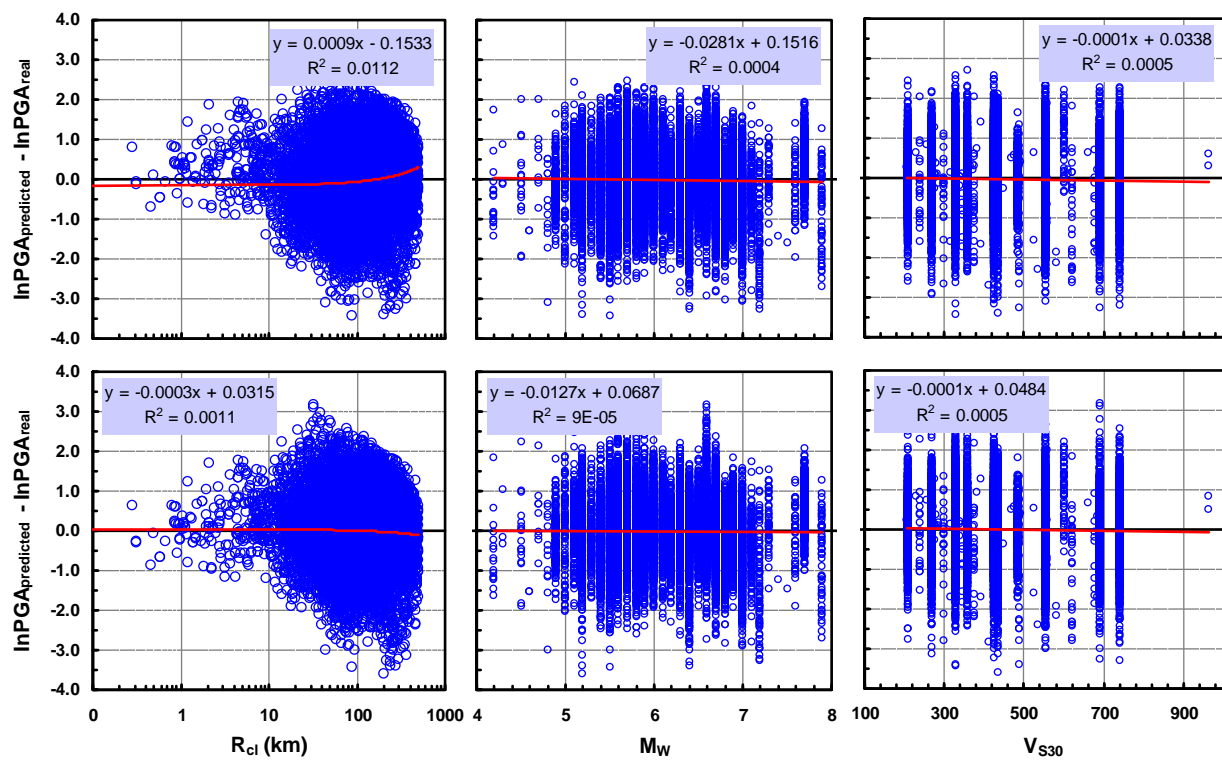


**Figure 8.**

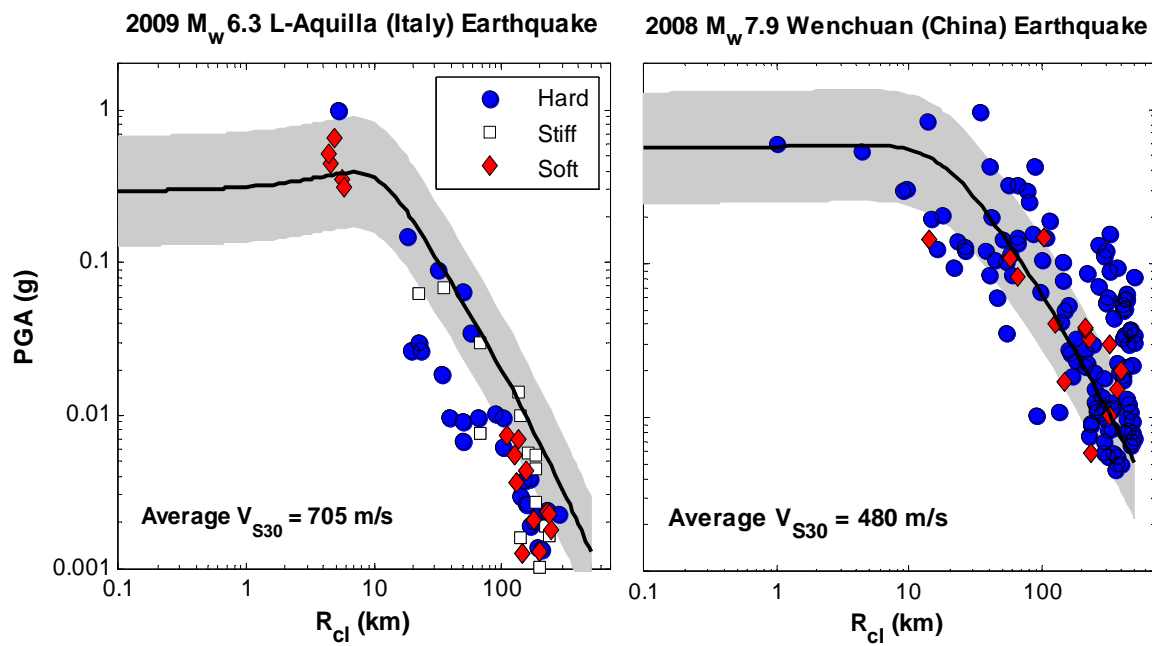


**Figure 9.**